

Energetic, tunable, highly elliptically polarized higher harmonics generated by intense two-color counter-rotating laser fields


Emmanouil Vassakis,^{1,2,*} Saibabu Madas^{3,4,*} Leandros Spachis,² Theocharis Lamprou,^{1,2} Ioannis Orfanos¹,¹ Subhendu Kahaly,³ Mousumi Upadhyay Kahaly,^{3,†} Dimitris Charalambidis,^{1,2,3} and Emmanouil Skantzakis^{1,‡}

¹*Foundation for Research and Technology - Hellas, Institute of Electronic Structure & Laser,
P.O. Box 1527, GR-71110 Heraklion (Crete), Greece*

²*Department of Physics, University of Crete, P.O. Box 2208, GR-71003 Heraklion (Crete), Greece*

³*ELI-ALPS, ELI-HU Non-Profit Ltd., Wolfgang Sandner utca 3, H-6728 Szeged, Hungary*

⁴*Institute of Physics, University of Szeged, Dóm tér 9, H-6720 Szeged, Hungary*

 (Received 5 May 2023; revised 5 August 2023; accepted 20 October 2023; published 13 November 2023; corrected 15 November 2023)

In this work, we demonstrate experimentally the efficient generation and tunability of energetic highly elliptical high harmonics in Ar gas, driven by intense two-color counter-rotating laser electric fields. A bichromatic beam tailored by a Mach-Zehnder-Less for Threefold Optical Virginia spiderwort (MAZEL-TOV) apparatus generates high-order harmonic generation (HHG), where the output spectrum of the highly elliptical HHG radiation can be tuned for an energy range of $\Delta E \approx 150$ meV in the spectral range of ~ 20 eV with energy per pulse $E^{\text{XUV}} \approx 400$ nJ at the source. Furthermore, we employ time-dependent density-functional simulations to probe the dependence of the harmonic ellipticity and the strength of the attosecond pulses on the driving-field parameters and demonstrate the robustness of the HHG with the bichromatic field. We show how, by properly tuning the central frequency of the second harmonic, the central frequency of the extreme ultraviolet (XUV) high-harmonic radiation is continuously tuned. The demonstrated energy values largely exceed the output energy from many other laser-driven attosecond sources reported so far and prove to be sufficient for inducing nonlinear processes in an atomic system. We envisage that such tunable energetic highly elliptical HHG spectra can remove the facility restrictions from requirements of few-cycle driving pulses for isolated circular attosecond-pulse generation.

DOI: [10.1103/PhysRevA.108.053112](https://doi.org/10.1103/PhysRevA.108.053112)

I. INTRODUCTION

Ultrafast chiral processes can be studied using high-order harmonic generation (HHG) [1–6]. HHG is an extreme nonlinear process which depends on many parameters, such as the nonlinear medium, the phase-matching conditions, the peak intensity, the duration, and the spectral phase of the driving pulse. By controlling these parameters it is possible to manipulate the spectral characteristics of the emitted extreme ultraviolet (XUV) radiation [7–10]. It has been demonstrated experimentally and theoretically that if we exploit different mechanisms, the harmonic HHG spectra can be influenced. Controlling parameters include the temporal chirp of the driving laser, the ionization-induced blueshift of the driver pulse in the generating medium [7,10,11], and the tuning of the central wavelength of the driver using an optical parametric amplifier [12]. HHG from linearly polarized drivers produces harmonics with linear polarization, and therefore, severe limitations are imposed on the potential applications of an XUV HHG source [13]. In this context, the development of a tunable highly elliptical XUV source removes this limitation.

Such sources recently emerged as a central topic of ultrafast science, promising invaluable insights into chiroptical phenomena taking place on ultrashort timescales. Ultra-short circularly polarized pulses in the XUV domain have been generated at large-scale facilities, such as free-electron lasers [14–16] and femto-sliced synchrotrons [17–19]. In an effort to make such sources more broadly available, tabletop sources based on HHG have also been developed [20–25].

The energy content of laser-driven highly elliptical or circularly polarized XUV radiation was limited to the picojoule range per pulse [20–23] until recently, when energy content in the nanojoule range was demonstrated in Ref. [24]. It is known that the recollision mechanism, which describes the HHG, requires that a stronger chiral response arises at the cost of a greatly suppressed high-harmonic emission signal [3]. Thus, the generation of energetic highly elliptical polarized high harmonics is also a decisive step towards chiral-matter investigations.

In the present work, tunable energetic highly elliptical HHG in the XUV regime is theoretically studied and experimentally demonstrated, exploiting two-color counter-rotating electric fields under loose focusing geometry. The output spectrum of the highly elliptical polarized HHG radiation can be tuned for an energy range of $\Delta E \approx 150$ meV in the spectral range of ~ 20 eV with energy per pulse $E^{\text{XUV}} \approx 400$ nJ at the source. This is, to our knowledge, the highest reported energy

*These authors contributed equally to this work.

†Corresponding author: mousumi.upadhyaykahaly@eli-alps.hu

‡Corresponding author: skanman@iesl.forth.gr

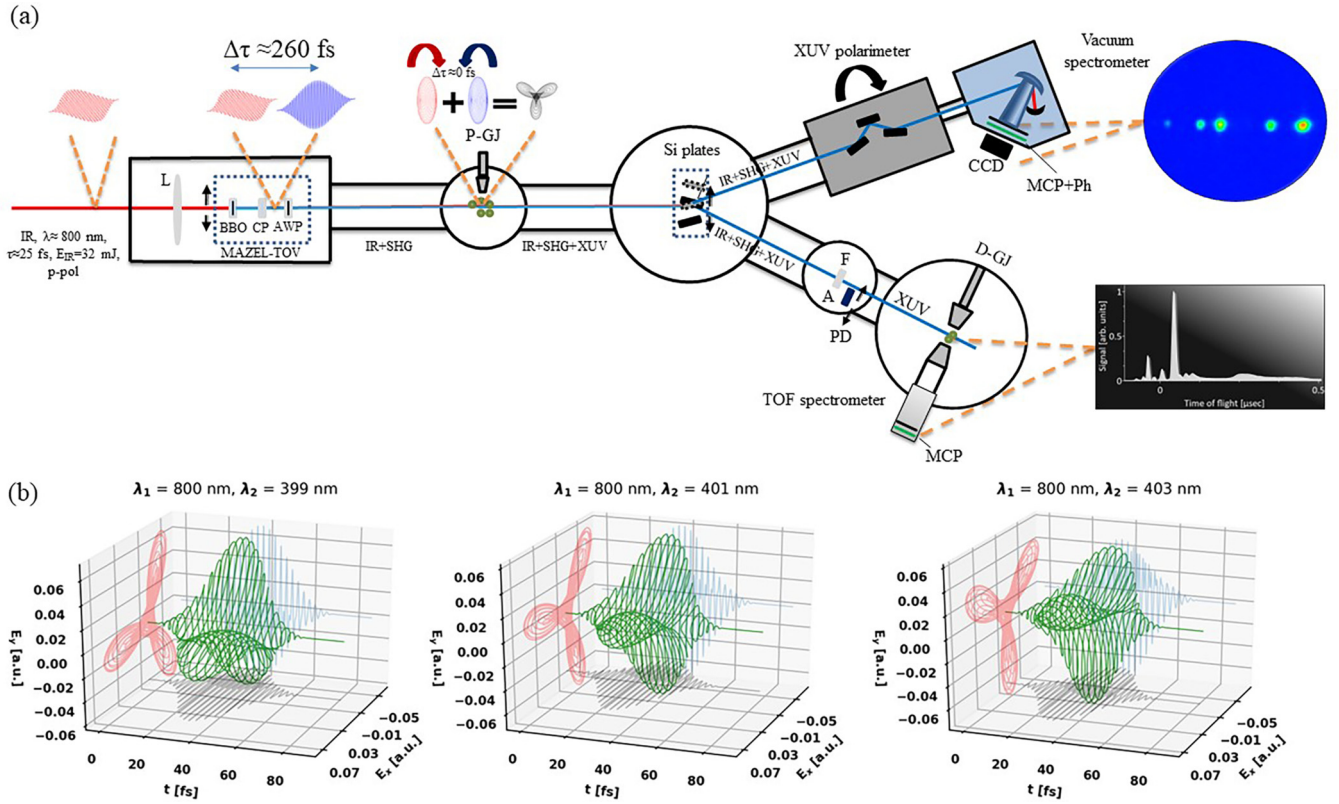


FIG. 1. (a) Experimental apparatus for the generation of highly elliptical polarized energetic tunable XUV radiation. A compact (15-cm-long) MAZEL-TOV-like device is installed after a 3-m focal length lens (L). The device includes a BBO crystal and a calcite plate (CP; both mounted independently on rotatable stages with high precision) and a rotatable superachromatic quarter-wave plate (AWP). The two-color bicircular field beam is focused into a pulsed gas jet filled with Ar (P-GJ). The generated XUV radiation is reflected towards the detection area by Si plates, which consists of two branches. The first branch hosts a calibrated XUV photodiode (PD), a pulsed gas jet filled with Ar (D-GJ), and, finally, a μ -metal shielded TOF spectrometer. The second branch hosts a rotating in-vacuum polarizer, and consequently, the XUV radiation is diffracted by a spherical holographic grating and detected by a microchannel-plate (MCP) detector coupled to a phosphor screen. (b) Calculated bicircular counter-rotating electric field formed at the output of the MAZEL-TOF-like device based on our experimental parameters, with fundamental field with a central wavelength λ_1 of 800 nm and three different second-harmonic field wavelengths λ_2 , i.e., 399, 401, and 403 nm.

content per laser pulse in the laser-driven highly elliptical, circularly polarized XUV radiation.

II. ADOPTED METHODOLOGIES: EXPERIMENTS AND SIMULATIONS

For the experimental implementation, a compact Mach-Zehnder-Less for Threefold Optical Virginia spiderwort-like (MAZEL-TOV-like [26]) scheme is used to generate elliptically polarized HHG spectra. The technique is detailed in Sec. II A and schematically described in Fig. 1(a). In order to understand the spectral and temporal structure of the generated high-order harmonics our experimental characterizations and results are supported by theoretical simulations based on a semiclassical approach, as elaborated in Sec. III D, and time-dependent density-functional theory, as discussed in Sec. III E, along with subcycle dynamics and crucial trends, revealing the factors in the estimated ellipticity of different harmonics.

A. Experimental setup

The experiment was performed by exploiting the Megawatt (MW) beamline of the Attosecond Science and Technology

Laboratory (AST) at Foundation for Research and Technology Hellas-Institute of Electronic Structure and Laser (FORTH-IESL). The experiment utilizes a 10-Hz-repetition-rate Ti:sapphire laser system delivering pulses with up to 400 mJ/pulse energy, $\tau_L = 25$ fs duration, and a carrier wavelength of 800 nm. The experimental setup consists of three areas: the focusing and MAZEL-TOV-like [26] device chamber, the harmonic-generation chamber, and the detection chambers (Fig. 1). A laser beam with a 3-cm outer diameter and an energy of 32 mJ/pulse passes through a 3-m-focal-length lens with the MAZEL-TOV-like device positioned 1.25 m downstream. The apparatus consists of a beta barium borate (BBO) crystal, a calcite plate, and a superachromatic quarter-wave plate. A fraction of the energy of the linear p -polarized fundamental pulse is converted into a perpendicularly polarized (s -polarized) second-harmonic field in a BBO crystal (0.2 mm, cutting angle of 29.20° for type-I phase matching). The conversion efficiency of the BBO crystal was maximized and it was found $\approx 30\%$ at 403 nm. The run-out introduced by the BBO crystal for the SHG of 800 nm was determined to be 38.6 fs. It is noted that by placing the BBO after the focusing lens ensures that the wave fronts of the

converging fundamental laser beam are reproduced into that of the second harmonic field. Therefore, the foci (placed close to a pulsed gas jet filled with Ar) of the ω and 2ω fields coincide along the propagation axis. Additionally, the beam passes through a calcite plate at almost normal incidence (AR coated, group velocity delay (GVD) compensation range 310-450 fs), which precompensates group delays introduced by the BBO crystal and the superachromatic quarter-wave plate. The superachromatic wave plate converts the two-color linearly polarized pump into a bicircular field, consisting of the fundamental field and its second harmonic, accumulating at the same time a group-delay difference of ~ 253 fs between the ~ 400 - and 800 -nm central wavelengths. Assuming Gaussian optics, the intensity at the focus for the two components of the bicircular polarized field is estimated to be $I_\omega \approx I_{2\omega} \approx 1 \times 10^{14}$ W/cm². After the jet, the produced XUV copropagates with the bicircular driving fields towards a pair of Si plates, which are placed at 75° , reducing the p -polarization component of the fundamental and second-harmonic radiation while reflecting the harmonics [27] towards the detection area. The detection area consists of two branches. In the first branch, which is placed directly after the first Si plate, a pair of 5-mm-diameter apertures were placed in order to block the outer part of the ω and 2ω beams while letting essentially the entire XUV through. A 150-nm-thick Sn filter is attached to the second aperture, not only for the spectral selection of the XUV radiation but also to eliminate the residual bicircular field. A calibrated XUV photodiode (XUV PD) can be introduced in the beam path in order to measure the XUV pulse energy. The transmitted beam enters the detection chamber, where the spectral characterization of the XUV radiation takes place. The characterization is achieved by recording the products of the interaction between the XUV beam and the Ar atoms. The electrons produced by the interaction of Ar atoms with the unfocused XUV radiation were detected by a μ -metal shielded time-of-flight (TOF) spectrometer. The spectral intensity distribution of the XUV radiation is obtained by measuring the single-photon ionization photoelectron (PE) spectra induced by the XUV radiation with photon energy higher than the ionization energy I_p of Ar ($I_{p\text{Ar}} = 15.76$ eV). In the second branch and after the Si plate, a rotating in-vacuum polarizer is installed, and consequently, the XUV radiation is diffracted by a spherical holographic grating and detected by a microchannel-plate (MCP) detector coupled with a phosphor screen.

B. Simulations

1. Semiclassical approach

In order to have an intuitive picture of the HHG by two-color bicircular polarized fields, we performed calculations based on the semiclassical approach, for which the theoretical framework and a detailed analysis can be found elsewhere [28]. In our Supplemental Material [29], we present an abbreviated analysis which is based on strong-field approximation (SFA) [30] adapted in the case of these electric fields.

Within this model, the radiation at orders $3n \pm 1$ (with $n = 1, 2, 3, \dots$) emitted from a single atom exposed to an intense bichromatic driving electric field $\mathbf{E}(t)$ with the associated

vector potential $A(t) = -\int \mathbf{E}(t)dt$ can be fully characterized by the Fourier transform of the time-dependent dipole moment. The details of this analysis can be found elsewhere [31].

2. Time-dependent density-functional formalism

The time-dependent electron dynamics in Ar under the influence of bichromatic counter-rotating (BCCR) laser fields is investigated based on *ab initio* calculation within time-dependent density-functional-theory (TDDFT) approach [32] in real-time and real-space grids as implemented in the OCTOPUS computational package [33,34]. Thus, a more detailed and a more complete picture of these dynamics is presented.

The driving laser fields, as described in terms of an electric field, are polarized in the x - y plane, and the dipole approximation is considered. In addition, the contributions from the magnetic component of the electromagnetic field and any other relativistic terms, such as spin-orbit coupling, are neglected. The combined electric field is a superposition of two counter-rotating laser fields and is given as

$$E(t) = \sum_{i=1,2} E_i \cos\left(\frac{(t - \tau_{\omega i})}{\tau_{\omega i}}\right)^2 \{ \cos[\omega_i(t - \tau_{\omega i})] \mathbf{e}_x + a_i \sin[\omega_i(t - \tau_{\omega i})] \mathbf{e}_y \}, \quad (1)$$

where \mathbf{e}_x and \mathbf{e}_y are the two mutually perpendicular unit vectors. We considered two counter-rotating fields of $a_1 = -a_2 = 1$ with $E_1 = E_2 = E_0$. The peak laser intensity is expressed in terms of field strength E_0 : $I = E_0^2 I_a$, where $I_a = 3.51 \times 10^{16}$ W/cm² is the atomic intensity unit. The peak intensity is $I = 1 \times 10^{14}$ W/cm². $\cos\left(\frac{(t - \tau_{\omega i})}{\tau_{\omega i}}\right)^2$ denotes the envelope of the pulse, where $\tau_{\omega 1}$ is the total duration of the fundamental pulse, which is defined in terms of the full width at half maximum of the intensity τ_p : $\tau_{\omega 1} = \tau_p / [2 \arccos(2^{-1/4})]$, where $\tau_p = 25$ fs. $\tau_{\omega 2}$ is the pulse duration of the second-harmonic field, which is defined as $\tau_{\omega 2} = \tau_{\omega 1} / \sqrt{2}$. A central wavelength $\lambda_1 = 800$ nm is used for the fundamental field, and four different wavelengths are used for the second-harmonic field, which are $\lambda_2 = 399, 400, 401, \text{ and } 403$ nm.

The initial states are obtained from self-consistent solutions of wave functions at the density-functional-theory (DFT) level. Later, those states are propagated by using the approximated enforced time-resolved-symmetry method, with $\Delta t = 0.3$ a.u. time steps. The rest of the TDDFT input parameters are presented in the Supplemental Material [29]. The harmonic spectral properties are calculated from the resulting dipole acceleration signal, which has components that are both parallel and perpendicular to the laser polarization. The harmonic spectrum $I(\omega)$ is obtained from the Fourier transformation of the time-dependent dipole acceleration $\mathbf{a}(t)$ and can be written as [35,36]

$$I(\omega) = \left| \mathcal{F} \left(\int_{-\infty}^{\infty} a(t) dt \right) \right|^2, \quad (2)$$

where \mathcal{FT} is the Fourier transform.

Three of the different bichromatic circularly polarized field variations with coplanar counter-rotating components that are used in both experiment and simulations in our work are shown in Fig. 1(b). Details of the TDDFT setup can be

found in [37–43], summarized in Sec. D of the Supplemental Material [29].

III. RESULTS AND ANALYSIS

A. Highly elliptical XUV radiation spectral characteristics

For the spectral characterization of the highly elliptical XUV radiation different PE spectra were recorded as a function of the angle $\Delta\theta$ of the BBO crystal installed in the MAZEL-TOV-like device. Characteristic highly elliptical HHG spectra are presented in Fig. 2(a) for three different positions of $\Delta\theta$. An energy shift is clearly observed towards higher photon energies when the angle $\Delta\theta$ between the propagation axis of the IR driving field and the BBO crystal is increased. Additionally, in Figs. 2(b)–2(e) complementary measurements of the detectable harmonics by the TOF spectrometer are presented. Finally, Fig. 2(f) presents highly elliptical HHG spectra obtained by the vacuum spectrometer for the sake of completeness. The maximum energy shift observed is on the order of $\Delta E \approx 150$ meV. It is revealed that the central HHG energy indicates an almost linear dependence on the central wavelength of the second harmonic generation (SHG). Note that the HHG spectra as recorded by TOF measurements and a vacuum spectrometer [see Figs. 2(a) and 2(f), respectively] are very different. The photon energy dependence of the efficiency and throughput of the two instruments differ depending on several parameters and effects. An important limitation is that the angular distribution of the photoelectrons, and hence the TOF throughput, is harmonically ellipticity dependent. Thus, a direct comparison of the ratio of the different shifted peaks is not physical. The observed blueshift can be attributed to the energy conservation of the HHG process by two-color BCCR electric fields. From energy conservation, the harmonic frequencies generated by these fields are given by

$$\Psi_{(n_1, n_2)} = n_1\omega + n_2\beta\omega, \quad (3)$$

where n_1 and n_2 are integer numbers that are associated with the number of photons involved in the process of HHG at angular frequencies ω and $\beta\omega$, respectively. On the other hand, parity and spin angular momentum conservation requires that $\Delta n = n_1 - n_2 = \pm 1$. Therefore, in the case of the 13th harmonic and $1.985 \leq \beta \leq 2.005$ (which reflects our experimental conditions), the unique pair (n_1, n_2) associated with this harmonic is equal to (5,4). It becomes evident that a linear dependence of the generated harmonic photon energy is expected as a function of the parameter β (as confirmed in Table I).

This dependence is depicted in Figs. 2(b)–2(e), with the green dashed lines calculated from the energy conservation of the annihilated driver photons and the emitted XUV photons (Table I) [44].

Note that the error bars in Figs. 2(b)–2(e) correspond to one standard deviation of the mean value of a series of measurements for each SHG central wavelength and for each harmonic. Within the error bars there is a slight deviation of the measured and theoretical values, which can be attributed to the strong IR central wavelength dependence of the calculation.

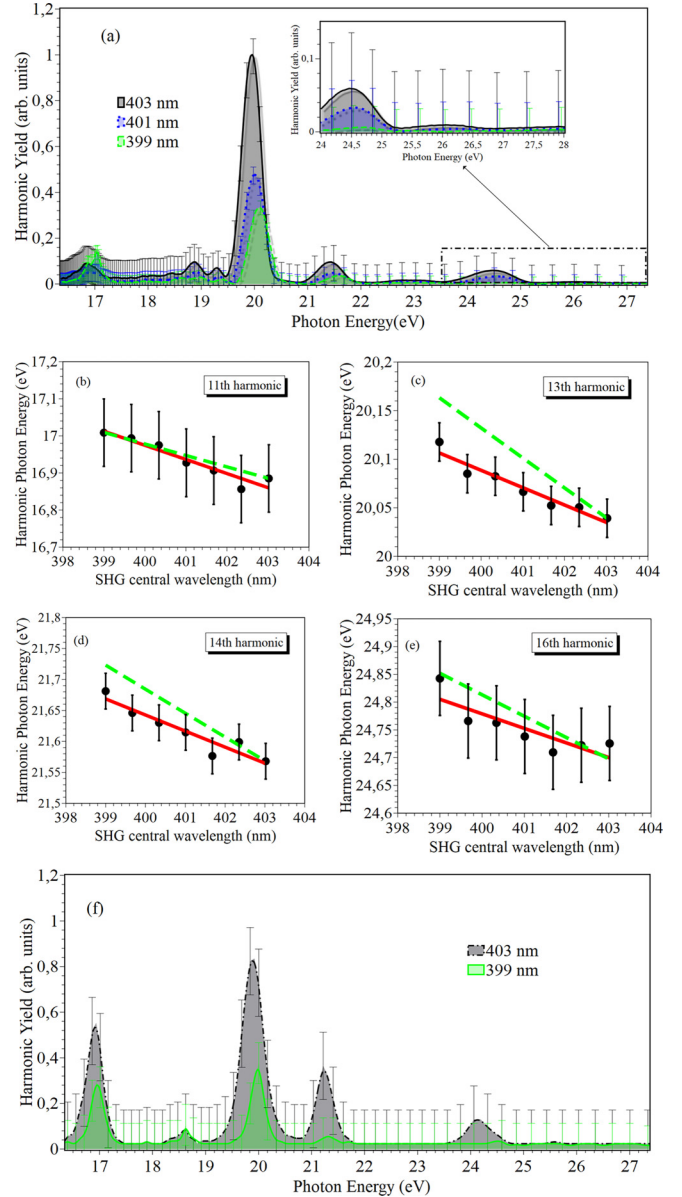


FIG. 2. (a) Characteristic highly elliptical polarized HHG spectra for three different values of the central SHG wavelength. The maximum energy shift observed is of the order of $\Delta E \approx 150$ meV. (b)–(e) Complementary analysis of the detectable harmonics (11th, 13th, 14th, and 16th, respectively). Linear dependence of the central HHG energy on the central wavelength of the SHG is observed. The green dashed line depicts the same dependence calculated from the energy conservation of the annihilated driver photons and the emitted XUV photon. (f) Highly elliptical HHG spectra obtained with the vacuum spectrometer.

From another perspective, this characteristic blueshift can be interpreted in the framework of the SFA [28,30]. The active electron acquires a different complex phase in the continuum for each central SHG wavelength. This leads to constructive interference at different spectral positions inside the HHG spectrum, resulting in the observed blueshift in the energy domain.

TABLE I. The slope $\Delta E/\Delta\lambda$ and q_{eff} involved in the interaction for each harmonic order. For each harmonic order, the corresponding channel is displayed in the second column, where n_1 is the number of photons of the fundamental field and n_2 is the number of photons of the second-harmonic field.

Harmonic	(n_1, n_2)	$\Delta E/\Delta\lambda$ (eV/nm)	q_{eff}
11th	(3, 4)	-0.03086	10.97 ± 2.74
13th	(5, 4)	-0.03086	8.62 ± 2.30
14th	(4, 5)	-0.03858	9.98 ± 2.63
16th	(6, 5)	-0.03858	12.38 ± 2.68
17th	(5, 6)	-0.04656	

The shift of the harmonics as a function of laser wavelength can be used in extracting the number of laser photons involved in the harmonic generation process, as performed spatially by Hickstein *et al.* [23]. Indeed, from the measured energy shift ΔE one can extract the equation of the photons involved in the interaction:

$$q_{\text{eff}} = \begin{cases} 3 \frac{\Delta E}{\Delta E_{\omega_2}} - 1, & \omega_q = 3q + 1, \\ 3 \frac{\Delta E}{\Delta E_{\omega_2}} + 1, & \omega_q = 3q - 1, \end{cases} \quad (4)$$

where $q = 1, 2, 3, \dots$, ΔE is the measured energy shift, and ΔE_{ω_2} is the corresponding energy shift of the second-harmonic frequency. q_{eff} for the detectable harmonics of our experiment is given in Table I.

B. Polarimetric investigation

The emitted harmonic radiation after the reflection of a Si plate is sent through a rotating in-vacuum polarizer, which consists of two UV-protected silver-coated mirrors and one UV-protected aluminum-coated mirror mounted on a common plate. The angle of incidence on each mirror is $75^\circ(\text{Ag})\text{-}60^\circ(\text{Al})\text{-}75^\circ(\text{Ag})$. Finally, the harmonic radiation is diffracted using a spherical holographic grating (platinum coated, 2400 G/mm) and detected by a MCP detector coupled to a phosphor screen. The contrast of the rotating in-vacuum polarizer was extracted by polarimetric measurements of the linear p -polarized XUV radiation (MAZEL-TOV-like device out of the beamline), which is presented in Fig. 3(a), and it was found to be $R = 2.2 \pm 0.1$ by fitting the imperfect polarizer equation under imperfect conditions [45] (for the mathematical extraction of the imperfect polarizer equation under perfect alignment see the Supplemental Material [29]).

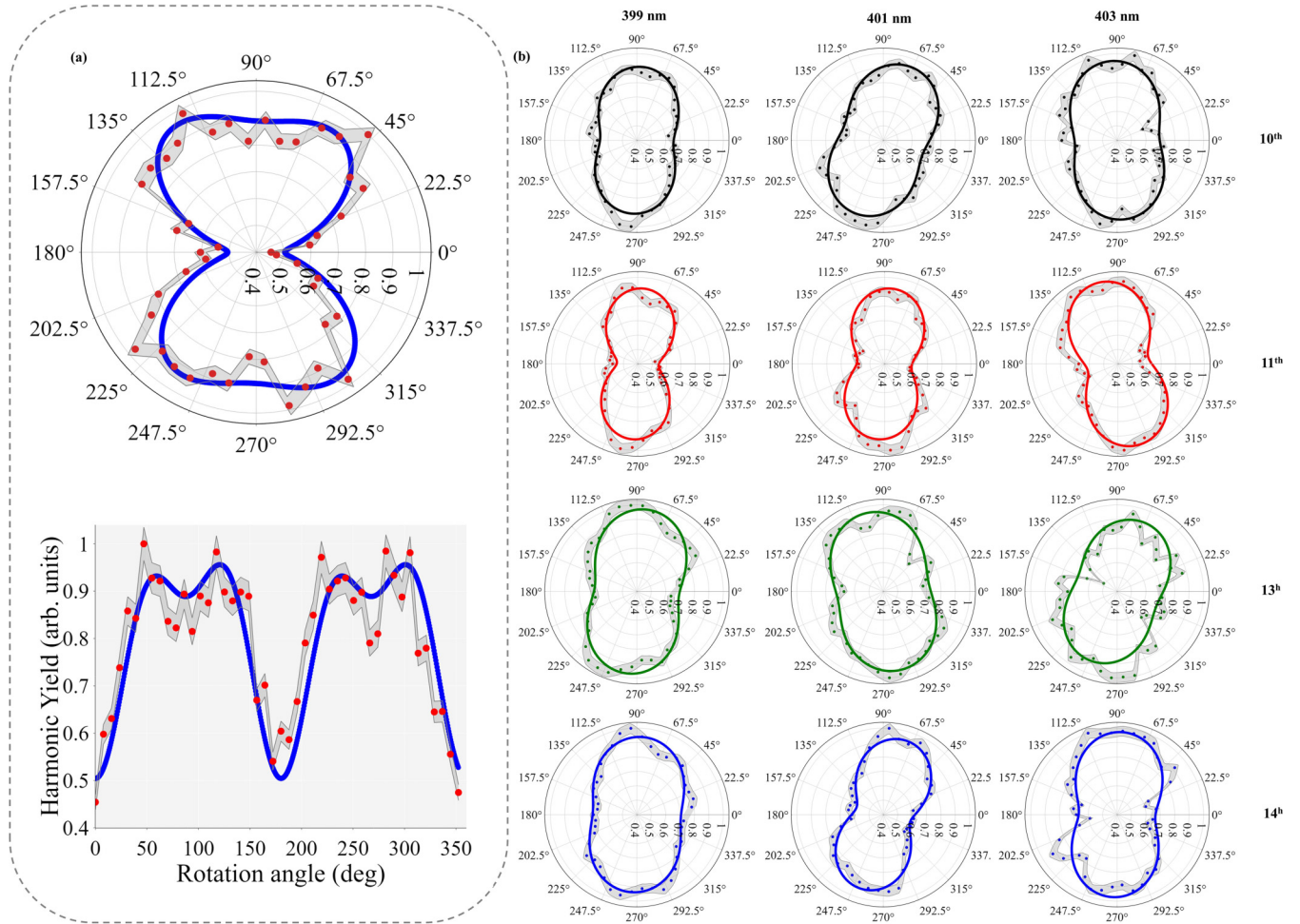


FIG. 3. (a) Characteristic polarimetric measurement for the 11th harmonic of the linear polarized driver. (b) Polarization scan for the 10th, 11th, 13th, and 14th harmonics used for three different values of the BBO tuning angle $\Delta\theta$ with respect to the propagation axis of the 25-fs IR laser pulse of the driver and thus different phase-matching SHG central wavelengths.

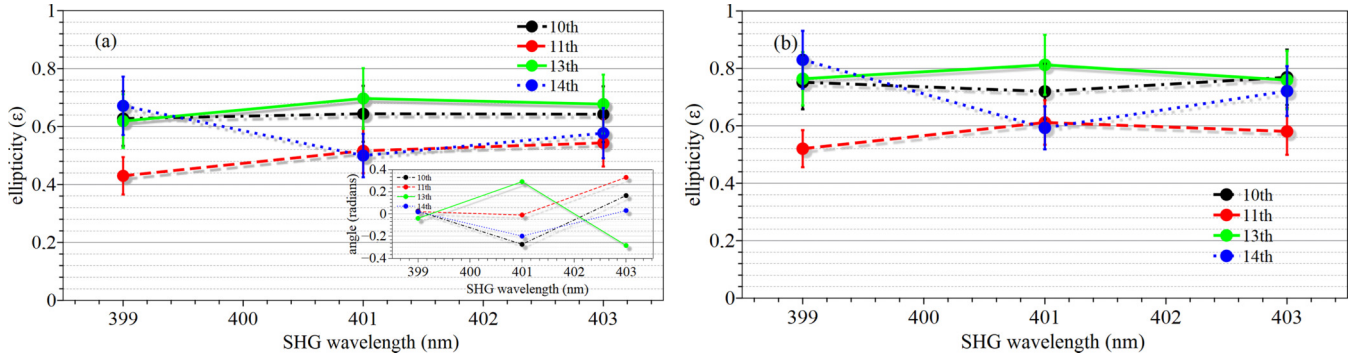


FIG. 4. (a) The dependence of ellipticity on the central wavelength of the SHG of the fundamental frequency in the *detection* area. The inset shows the angle between the ellipsis major axis and the vector perpendicular to the polarization axis of the linearly polarized field. (b) The reconstructed ellipticity values at the *source*. The error bars correspond to one standard deviation of the mean value of a series of polarimetric investigations for each SHG central wavelength and for each harmonic.

Polarimetric measurements were performed for the 10th, 11th, 13th, and 14th harmonics as a function of the angle $\Delta\theta$. Therefore, polarization scans were acquired during which the polarizer was rotated between 0° and 360° in steps of $\sim 8^\circ$ with an average of 40 pulses per step.

From these scans the ellipticity of the high harmonics as a function of the BBO angle was derived. The measurement of the state of polarization of the HHG spectra confirmed highly elliptical polarization reaching ellipticities up to $\sim 70\%$ at ~ 22 eV, as presented in Fig. 4(a). No dependence on the central wavelength of the SHG was found. Briefly, the polarization state of these highly elliptical polarized harmonics was extracted by fitting the imperfect polarizer equation [Eq. (10) of the Supplemental Material [29]] to the raw data of the polarization scans, keeping as the only known parameter the contrast of the polarizer $R = 2.2 \pm 0.1$. The angle between the ellipsis major axis and the vector perpendicular to the polarization axis of the linearly polarized field resulting from the polarimetric measurements is shown in the inset of Fig. 4(a). The direction of the ellipse is strongly dependent (i) only on the phase of the XUV radiation and the delay between the two-color counter-rotating fields (which can be adjusted experimentally by rotating the angle of the calcite plate in the MAZEL-TOV device) at a constant second-harmonic wavelength and (ii) on the BBO angle if all other parameters are kept constant. This results in tuning two experimental parameters, (i) the central wavelength and the amplitude of the second-harmonic field and (ii) the delay between the fundamental and second-harmonic fields, by a small amount. Both experimental parameters result in a rotation of the rosette field along the propagation axis. At the same time the harmonic phase changes since the components of the electric field have different energy ratios. Details can be found in [46].

In the present configuration used for the characterization of the harmonic ellipticity the Si plate reflects the harmonic radiation to the XUV polarimeter. This optical component provides marginally different reflectivity for the *s*- and *p*-polarization components of the XUV radiation, also affecting the measured ellipticity of the HHG radiation. By calculating the reflectivity of the Si plate for the two polarization orientations using the corresponding Fresnel equations and the refractive indices taken from Palik [47], for each harmonic

component, the values of ellipticity at the *source* can be estimated. Ellipticities up to $\sim 85\%$ at ~ 22 eV were found, as shown in Fig. 4(b). These ellipticity values in conjunction with the high-energy content of the XUV pulses reveal a source adequate for applications like control and imaging of ultrafast magnetism in magnetic materials [48–50], in ultrafast chiral matter investigations [22], and also in the investigation of circular dichroism in atomic systems [51–53] in which intense highly elliptical or circularly polarized XUV radiation is necessary for inducing nonlinear processes [52].

C. Energy-content estimation

The energy content of the XUV radiation was estimated by applying an experimental procedure similar to the one reported by Vassakis *et al.* [24], and it was found to be $E^{\text{XUV}} \approx 400$ nJ per XUV pulse at the source. Briefly, the energy of the highly elliptical polarized XUV radiation emitted per pulse is estimated at a first step by measuring the linearly polarized XUV pulse energy by means of an XUV photodiode and comparing the HHG spectra depicted in the measured photoelectron spectrum of Ar atoms upon interaction with highly elliptically and linearly polarized XUV light (see Fig. 5) under the same detection conditions. Additionally, the single-photon photoelectron angular distributions were taken into account for each harmonic in the case of Ar [54] in order to check how they affect the detection in the case of

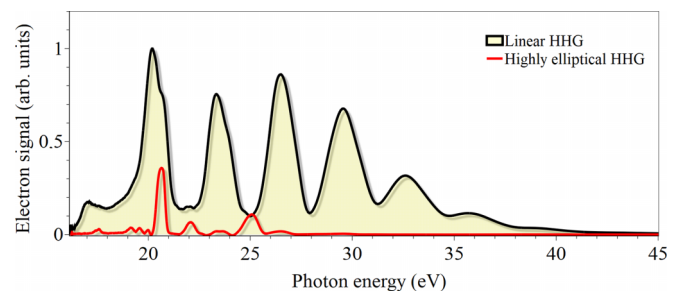


FIG. 5. Typical PE spectra of Ar induced by the linear *p*-polarized and highly elliptical XUV radiation generated by Ar under the same detection conditions after the optimization of harmonic emission is realized in both cases.

TABLE II. Number of photons per harmonic order per pulse at the source when Ar is used as the generating medium.

Harmonic order	No. of photons per pulse
11th	$\sim 1.4 \times 10^{10}$
13th	$\sim 8.4 \times 10^{10}$
14th	$\sim 8 \times 10^9$
16th	$\sim 2.3 \times 10^9$
17th	$\sim 3.2 \times 10^8$

our experimental configuration. From all of the above, we can deduce the energy per pulse of the highly elliptically polarized XUV emission. This major improvement with respect to the previous reported value (~ 100 nJ at the source) [24] is due to the improvement of the focusing conditions and the increased input laser energy (32 mJ) of the terawatt 10-Hz laser system. It should be stressed that no depletion of the atomic target (Ar) was observed during these experimental investigations, and therefore, a higher energy content of highly elliptical XUV radiation is expected from increasing the input energy. Therefore, the limit for the driving laser energy was set by the possible damage threshold of the optical components. The estimated number of photons per harmonic per pulse at the source is shown in Table II.

D. Semiclassical analysis of HHG spectra and phases

According to the semiclassical approach, the HHG from bicircular harmonic fields has different characteristics than the case of linearly monochromatic polarized driver fields. Reference [28] showed that the main contribution to the harmonic emission comes from electrons with $\text{Re}(t) < \frac{T_L}{3}$ (where T_L is the fundamental laser period). Here it should be stressed that because of the threefold electric field which is raised by the superposition of the bicircular electric fields, primarily, one trajectory contributes during the process of HHG, in contrast to the case of linear monochromatic drivers, in which two trajectories contribute to harmonic emission, namely, *short* and *long* [55–58].

Figure 6(a) represents the harmonic phase of the $3n \pm 1$ harmonics ($n = 4, 5$) as a function of the intensity in the case where $I_\omega = I_{2\omega}$. The Ar atomic target is used as the generation medium. The result is that the slope of the phase as a function of the intensity for each harmonic is *small*. This is indicative of a *strong collective response* when loose focusing geometry is applied [20,44,59–61]. For equal intensities of the laser field's components $I_\omega = I_{2\omega}$ the cutoff law is $E_{\text{max}} = 1.2I_p + 3.17U_p$, where $U_p = U_{p\omega} + U_{p2\omega}$ [28,62].

With this semiclassical three-step model [28,30,63,64], the HHG spectrum was also calculated for different SHG central wavelengths ($399 \leq \lambda_2 \leq 403$ nm). It is shown here theoretically [Fig. 6(b)] and verified experimentally in Sec. III A that the harmonic photon energy follows a linear dependence on the SHG central wavelength.

E. Probing the dynamical origin of the high-ellipticity harmonics with TDDFT

In this work, the peak intensities of the fundamental and second-harmonic fields are taken as 1×10^{14} W/cm². As

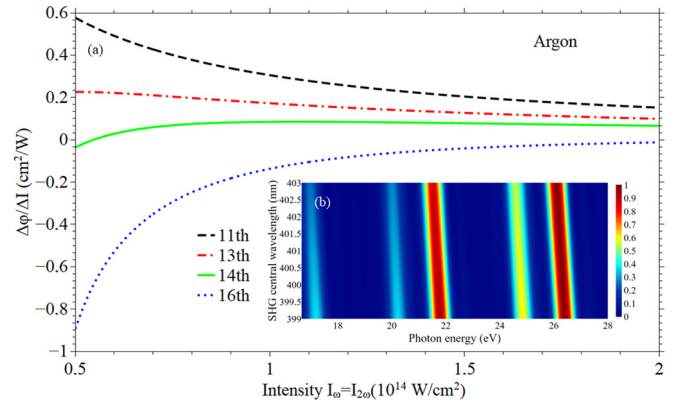


FIG. 6. (a) Harmonic phase of the $3n \pm 1$ harmonics ($n = 4, 5$) as a function of the intensity of the two components of the bicircular counter-rotating fields. Parameters used in the calculations are laser central wavelength of 800 nm, 400-nm second harmonic, and pulse peak intensity $I_\omega = I_{2\omega}$ for argon. (b) Harmonic spectra as a function of the SHG central wavelength. Parameters used in the calculations are fundamental central wavelength $\lambda_1 = 800$ nm, second-harmonic central wavelength tuned in the range $399 \leq \lambda_2 \leq 403$ nm, and pulse peak intensity $I_\omega = I_{2\omega} = 1 \times 10^{14}$ W/cm² for argon.

shown in Fig. 1(b) the total electric field has a trefoil pattern. The harmonic generation and tunability of the photon energy of the emitted harmonics in the Ar atom is obtained by combining a circularly polarized light with a fundamental frequency ω_1 ($\lambda_1 = 800$ nm) with its counter-rotating second-harmonic ω_2 ($\lambda_2 = 399, 400, 401, \text{ or } 403$ nm). The harmonic radiation is plotted as the sum of the absolute square of the two polarization components (x and y), as shown in linear and logarithmic scale in Figs. 7(a) and 7(b), respectively. The HHG spectrum in Fig. 7(b) displays a distinct structural peak in the lower frequency range of 15–30 eV.

We find that the emitted harmonic spectral features, such as the HHG intensity and the polarization states of the harmonics, show strong dependence on the wavelength and intensity ratio of the two driving-field components in the BCCR field. The dependence of the generated harmonic spectrum on the SHG central wavelength, as obtained from our TDDFT analysis, shows very good agreement with the theoretical calculations presented in Sec. III D. A maximum HHG central energy shift of ~ 150 meV is also observed by tuning the second-harmonic wavelength, as shown in Fig. 7(a), supporting the experimental results in Sec. III A.

We investigate how the ellipticity of the emitted harmonics varies as a function of the second-harmonic wavelength. For illustration purposes we show for $\lambda_2 = 401$ nm the ellipticity of the 14th emitted harmonic in Fig. 8(a). As shown in Fig. 8(b), a super-Gaussian filter is applied around the 14th-harmonic field (red curve), which is shown in Fig. 8(c). A slice at the peak of the harmonic field is selected, and an ellipse is fitted to it (blue dashed curve). By taking the ratio of semiminor and semimajor axes, the ellipticity is calculated. The dependence of the second-harmonic field wavelength on the ellipticity of the emitted harmonics is shown in Fig. 8(d).

We observe that by using the peak intensities of the fundamental field (1×10^{14} W/cm²), the harmonic ellipticity corresponding to the BCCR field-induced HHG emission is

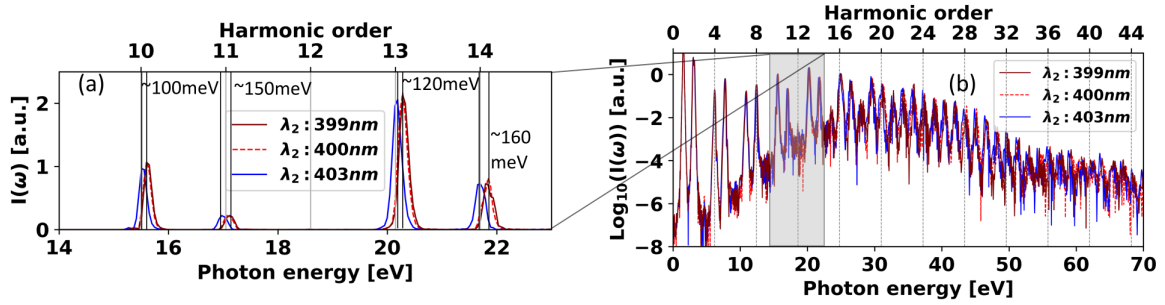


FIG. 7. High-order harmonic spectra of an Ar atom in (a) linear scale and (b) logarithmic scale obtained under the influence of a BCCR laser field. A wavelength of $\lambda_1 = 800$ nm for the fundamental laser field is fixed, and the wavelengths of the second-harmonic field are varied, i.e., $\lambda_2 = 399, 400,$ and 403 nm. The energy shift in the high-order harmonic spectra as a function of the second-harmonic laser field's wavelength is shown in (a).

significantly reduced for all harmonic orders detectable in the TOF spectrometer, indicating prominent depolarization effects. In particular, by examining harmonic orders 10 to 14 [see Fig. 8(d)], we find that the calculated ellipticity varies from 0.65 to 0.98, the same as in our experimental results, without showing any predictable particular order, while the 10th and 13th harmonics show a close-to-circularity elliptic nature. The estimated degree of polarization of individual harmonic orders exhibits gross features and magnitudes similar to those obtained from our experimental results.

The combined electric field of the bicircular field has a threefold rosette shape [Fig. 1(b)]. The electron wave packets released through tunnel ionization close to each field

maximum are accelerated and finally recollide with the parent ion every $1/3$ of the ω cycle [28]. In an isotropic and time-independent medium, this leads to the emission of attosecond pulses of equal intensity every $T/3$, linearly polarized (along the recollision direction) with orientation increasing by 120° every $T/3$ [65]. This threefold dynamical symmetry imposes emission of only the $3n \pm 1$ (with $n = 1, 2, 3, \dots$) harmonic orders with circular polarization [20,28]. Some examples of breaking this dynamical symmetry include (i) amplitudes that are not exactly equal and imperfect overlap of the ω and 2ω fields in the experiment [66], (ii) deviation from zero delay between the ω and 2ω pulses in the experiment, and (iii) macroscopic effects [20,67]. Any breaking of symmetry

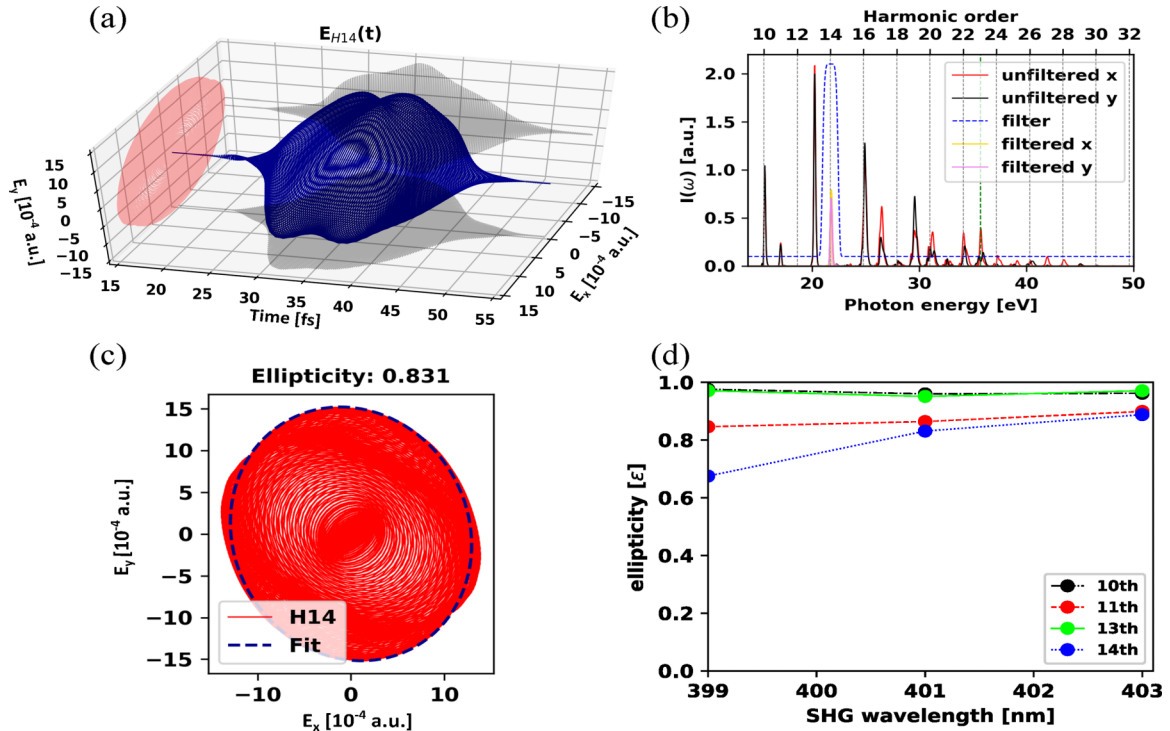


FIG. 8. High-order harmonic generation from Ar using a BCCR laser field with $\lambda_1 = 800$ nm and $\lambda_2 = 401$ nm. (a) Temporal evolution of the ellipticity of the emitted harmonics super-Gaussian filtered around the 14th harmonic. (b) Computed HHG spectrum from the Ar super-Gaussian filtered (blue curve) around the 14th harmonic. The green vertical dashed line is the harmonic cutoff. (c) The resulting harmonic field of the filtered harmonics (in red) is sliced at its maximum and fitted to an ellipse (in blue). (d) Effect of the second-harmonic frequency on the ellipticity of the harmonics.

between the three attopulses in the ω cycle would result in a decreased harmonic ellipticity, emission of the $3q$ harmonic orders, and possibly depolarization [66]. The difference in the ellipticity values derived from the experimental data in Fig. 4 and those extracted from TDDFT calculations in Fig. 8(d) can be attributed to the use of ideal conditions in the theory which are not met in the actual experiment as they are described above. It is worth noting that our experimental approach cannot distinguish between circularly polarized and nonpolarized radiation, thus, small contributions of nonpolarized harmonics are inevitable. As shown in [66], such breaking can occur even for perfectly circular driving fields and in an isotropic medium, when the strong-field interaction leading to the harmonic emission presents subcycle modulations due to (i) fast temporal variation of the driving laser fields on the envelope's rising and falling edges, causing temporal variations of the harmonic dipole vector, and (ii) ionization of the medium resulting in a fast decay of the induced dipole strength with time. Such effects are also not taken into account in the TDDFT calculations, which thus results in the maximum possible ellipticity.

IV. CONCLUSIONS

In conclusion, we reported a method to produce tunable energetic highly elliptical XUV radiation. The approach is based on gas-phase HHG driven by two-color bicircular polarized fields, produced by a MAZEL-TOV-like device. The approach was applied at the linearly polarized MW XUV beamline at FORTH-IESL under loose focusing conditions. By properly tuning the central frequency of the second harmonic of the fundamental frequency, the central frequency of the XUV HHG can be continuously tuned. By performing polarimetric measurements, ellipticities up to $\sim 85\%$ at ~ 22 eV were achieved. No clear dependence on the BBO angle of rotation was observed. The energy per driving laser pulse in the spectral region ≈ 20 eV was found to be in the range of $E^{\text{XUV}} \approx 400$ nJ per laser pulse at the source. The maximum energy shift observed was $\Delta E \approx 150$ meV, which is in good agreement with the theoretical calculations.

Overall, by combining state-of-the-art experiments, semi-classical analysis, and TDDFT simulations, we demonstrated efficient generation and characterization of highly energetic and elliptic high-harmonic spectra from Ar and also identified

the dynamical origin and spectral, temporal nature of the generated elliptic high-order harmonics. We found that the proposed technique to generate and tune the BCCR field under suitable focusing conditions can result in highly energetic (400 nJ at the source) elliptically polarized harmonic spectra, with a linear dependence of the central HHG energy on the central wavelength of the SHG. While certain harmonic regions demonstrate a high degree of ellipticity (almost tending to circularity, for example, the 10th and 13th harmonics), other detectable high harmonics demonstrate lower ellipticity. Similar features were also confirmed with our TDDFT simulations. By suitably tuning and improving the focusing conditions, we could achieve a high value of the energy content per pulse of the highly elliptical XUV emission (400 nJ at the source), which is much higher than previously reported results. Hence, employing our approach based on a short-pulse driving laser and by varying the SHG central wavelength, it is possible to achieve spatially varying elliptically polarized high harmonics that can be utilized in imaging and spectroscopic applications in the materials [68], chemical, and nanosciences [69], as well as to probe chirality-sensitive processes.

ACKNOWLEDGMENTS

We acknowledge support for this work from the LASERLAB-EUROPE (EU's Horizon 2020 Grant No. 871124), the IMPULSE project (Grant No. 871161), the Hellenic Foundation for Research and Innovation (HFRI), and the General Secretariat for Research and Technology (GSRT) under GAICPEU (Grant No. 645) and Grant Agreement No. NEA-APS HFRI-FM17-2668. ELI-ALPS is supported by the European Union and cofinanced by the European Regional Development Fund (Grant No. GINOP-2.3.6-15-2015-00001). This research was supported by the IMPULSE project, which receives funding from the European Union Framework Programme for Research and Innovation Horizon 2020 under Grant Agreement No. 871161. S.K., S.M., and M.U.K. also acknowledges Project No. 2019-2.1.13-TÉT-IN-2020-00059, which was implemented with support provided by the National Research, Development and Innovation Fund of Hungary and financed under the 2019-2.1.13-TÉT-IN funding scheme. S.M. and M.U.K. would like to acknowledge ELI-ALPS HPC administration for their support in providing computational resources.

-
- [1] D. Baykusheva and H. J. Wörner, Chiral discrimination through bielliptical high-harmonic spectroscopy, *Phys. Rev. X* **8**, 031060 (2018).
 - [2] D. Ayuso, O. Neufeld, A. F. Ordonez, P. Declava, G. Lerner, O. Cohen, M. Ivanov, and O. Smirnova, Synthetic chiral light for efficient control of chiral light-matter interaction, *Nat. Photon.* **13**, 866 (2019).
 - [3] R. Cireasa, A. E. Boguslavskiy, B. Pons, M. C. H. Wong, D. Descamps, S. Petit, H. Ruf, N. Thiré, A. Ferré, J. Suarez, J. Higuette, B. E. Schmidt, A. F. Alharbi, F. Légraré, V. Blanchet, B. Fabre, S. Patchkovskii, O. Smirnova, Y. Mairesse, and V. R. Bhardwaj, Probing molecular chirality on a sub-femtosecond timescale, *Nat. Phys.* **11**, 654 (2015).
 - [4] T. Heinrich, M. Taucer, O. Kfir, P. B. Corkum, A. Staudte, C. Ropers, and M. Siviş, Chiral high-harmonic generation and spectroscopy on solid surfaces using polarization-tailored strong fields, *Nat. Commun.* **12**, 3723 (2021).
 - [5] O. Neufeld and O. Cohen, Optical chirality in nonlinear optics: Application to high harmonic generation, *Phys. Rev. Lett.* **120**, 133206 (2018).
 - [6] O. Neufeld, D. Ayuso, P. Declava, M. Y. Ivanov, O. Smirnova, and O. Cohen, Ultrasensitive chiral spectroscopy by dynamical symmetry breaking in high harmonic generation, *Phys. Rev. X* **9**, 031002 (2019).
 - [7] C. Altucci, T. Starczewski, E. Mevel, C.-G. Wahlström, B. Carré, and A. L'Huillier, Influence of atomic density in high-order harmonic generation, *J. Opt. Soc. Am. B* **13**, 148 (1996).

- [8] Z. Chang, A. Rundquist, H. Wang, I. Christov, H. C. Kapteyn, and M. M. Murnane, Temporal phase control of soft-x-ray harmonic emission, *Phys. Rev. A* **58**, R30(R) (1998).
- [9] D. G. Lee, J.-H. Kim, K.-H. Hong, and C. H. Nam, Coherent control of high-order harmonics with chirped femtosecond laser pulses, *Phys. Rev. Lett.* **87**, 243902 (2001).
- [10] C. Winterfeldt, C. Spielmann, and G. Gerber, Colloquium: Optimal control of high-harmonic generation, *Rev. Mod. Phys.* **80**, 117 (2008).
- [11] C. A. Froud, E. T. Rogers, D. C. Hanna, W. S. Brocklesby, M. Praeger, A. M. de Paula, J. J. Baumberg, and J. G. Frey, Soft-x-ray wavelength shift induced by ionization effects in a capillary, *Opt. Lett.* **31**, 374 (2006).
- [12] B. Shan, A. Cavalieri, and Z. Chang, Tunable high harmonic generation with an optical parametric amplifier, *Appl. Phys. B* **74**, s23 (2002).
- [13] K. Chordiya, V. Despré, B. Nagyllés, F. Zeller, Z. Diveki, A. I. Kuleff, and M. U. Kahaly, Photo-ionization initiated differential ultrafast charge migration: Impacts of molecular symmetries and tautomeric forms, *Phys. Chem. Chem. Phys.* **25**, 4472 (2023).
- [14] B. W. J. McNeil and N. R. Thompson, X-ray free-electron lasers, *Nat. Photon.* **4**, 814 (2010).
- [15] D. J. Higley *et al.*, Femtosecond x-ray magnetic circular dichroism absorption spectroscopy at an x-ray free electron laser, *Rev. Sci. Instrum.* **87**, 033110 (2016).
- [16] A. A. Lutman *et al.*, Polarization control in an x-ray free-electron laser, *Nat. Photon.* **10**, 468 (2016).
- [17] S. Khan, K. Holldack, T. Kachel, R. Mitzner, and T. Quast, Femtosecond undulator radiation from sliced electron bunches, *Phys. Rev. Lett.* **97**, 074801 (2006).
- [18] N. Yamamoto, M. Shimada, M. Adachi, H. Zen, T. Tanikawa, Y. Taira, S. Kimura, M. Hosaka, Y. Takashima, T. Takahashi, and M. Katoh, Ultra-short coherent terahertz radiation from ultra-short dips in electron bunches circulating in a storage ring, *Nucl. Instrum. Methods Phys. Res., Sect. A* **637**, S112 (2011).
- [19] N. Čutić, F. Lindau, S. Thorin, S. Werin, J. Bahrtdt, W. Eberhardt, K. Holldack, C. Erny, A. L'Huillier, and E. Mansten, Vacuum ultraviolet circularly polarized coherent femtosecond pulses from laser seeded relativistic electrons, *Phys. Rev. Spec. Top. Accel. Beams* **14**, 030706 (2011).
- [20] O. Kfir, P. Grychtol, E. Turgut, R. Knut, D. Zusin, D. Popmintchev, T. Popmintchev, H. Nembach, J. M. Shaw, A. Fleischer, H. Kapteyn, M. Murnane, and O. Cohen, Generation of bright phase-matched circularly-polarized extreme ultraviolet high harmonics, *Nat. Photon.* **9**, 99 (2015).
- [21] A. Comby, E. Bloch, S. Beauvarlet, D. Rajak, S. Beaulieu, D. Descamps, A. Gonzalez, F. Guichard, S. Petit, Y. Zaouter, V. Blanchet, and Y. Mairesse, Bright, polarization-tunable high repetition rate extreme ultraviolet beamline for coincidence electron-ion imaging, *J. Phys. B* **53**, 234003 (2020).
- [22] A. Ferré, C. Handschin, M. Dumergue, F. Burgy, A. Comby, D. Descamps, B. Fabre, G. A. Garcia, R. Géneaux, L. Merceron, E. Mével, L. Nahon, S. Petit, B. Pons, D. Staedter, S. Weber, T. Ruchon, V. Blanchet, and Y. Mairesse, A table-top ultrashort light source in the extreme ultraviolet for circular dichroism experiments, *Nat. Photon.* **9**, 93 (2015).
- [23] D. D. Hickstein, F. J. Dollar, P. Grychtol, J. L. Ellis, R. Knut, C. Hernández-García, D. Zusin, C. Gentry, J. M. Shaw, T. Fan, K. M. Dorney, A. Becker, A. Jaroń-Becker, H. C. Kapteyn, M. M. Murnane, and C. G. Durfee, Non-collinear generation of angularly isolated circularly polarized high harmonics, *Nat. Photon.* **9**, 743 (2015).
- [24] E. Vassakis, I. Orfanos, I. Lontos, and E. Skantzakis, Generation of energetic highly elliptical extreme ultraviolet radiation, *Photonics* **8**, 378 (2021).
- [25] A. Comby, D. Rajak, D. Descamps, S. Petit, V. Blanchet, Y. Mairesse, J. Gaudin, and S. Beaulieu, Ultrafast polarization-tunable monochromatic extreme ultraviolet source at high-repetition-rate, *J. Opt.* **24**, 084003 (2022).
- [26] O. Kfir, E. Bordo, G. Ilan Haham, O. Lahav, A. Fleischer, and O. Cohen, In-line production of a bi-circular field for generation of helically polarized high-order harmonics, *Appl. Phys. Lett.* **108**, 211106 (2016).
- [27] E. J. Takahashi, H. Hasegawa, Y. Nabekawa, and K. Midorikawa, High-throughput, high-damage-threshold broadband beam splitter for high-order harmonics in the extreme-ultraviolet region, *Opt. Lett.* **29**, 507 (2004).
- [28] D. B. Milosevic, W. Becker, and R. Kopold, Generation of circularly polarized high-order harmonics by two-color coplanar field mixing, *Phys. Rev. A* **61**, 063403 (2000).
- [29] See Supplemental Material at <http://link.aps.org/supplemental/10.1103/PhysRevA.108.053112> for the experimental and theoretical technical details supporting the corresponding results presented in the main text.
- [30] M. Lewenstein, P. Balcou, M. Y. Ivanov, A. L'Huillier, and P. B. Corkum, Theory of high-harmonic generation by low-frequency laser fields, *Phys. Rev. A* **49**, 2117 (1994).
- [31] A. Nayak *et al.*, Saddle point approaches in strong field physics and generation of attosecond pulses, *Phys. Rep.* **833**, 1 (2019).
- [32] E. Runge and E. K. U. Gross, Density-functional theory for time-dependent systems, *Phys. Rev. Lett.* **52**, 997 (1984).
- [33] X. Andrade, J. Alberdi-Rodriguez, D. A. Strubbe, M. J. T. Oliveira, F. Nogueira, A. Castro, J. Muguerza, A. Arruabarrena, S. G. Louie, A. Aspuru-Guzik, A. Rubio, and M. A. L. Marques, Time-dependent density-functional theory in massively parallel computer architectures: the octopus project, *J. Phys. Condens. Matter* **24**, 233202 (2012).
- [34] X. Andrade, D. Strubbe, U. D. Giovannini, A. H. Larsen, M. J. T. Oliveira, J. Alberdi-Rodriguez, A. Varas, I. Theophilou, N. Helbig, M. J. Verstraete, L. Stella, F. Nogueira, A. Aspuru-Guzik, A. Castro, M. A. L. Marques, and A. Rubio, Real-space grids and the octopus code as tools for the development of new simulation approaches for electronic systems, *Phys. Chem. Chem. Phys.* **17**, 31371 (2015).
- [35] X. Chu and S.-I. Chu, Time-dependent density-functional theory for molecular processes in strong fields: Study of multi-photon processes and dynamical response of individual valence electrons of N₂ in intense laser fields, *Phys. Rev. A* **64**, 063404 (2001).
- [36] K. Burnett, V. C. Reed, J. Cooper, and P. L. Knight, Calculation of the background emitted during high-harmonic generation, *Phys. Rev. A* **45**, 3347 (1992).
- [37] A. Castro, M. A. L. Marques, and A. Rubio, Propagators for the time-dependent Kohn-Sham equations, *J. Chem. Phys.* **121**, 3425 (2004).
- [38] M. A. Marques, M. J. Oliveira, and T. Burnus, Libxc: A library of exchange and correlation functionals for density functional theory, *Comput. Phys. Commun.* **183**, 2272 (2012).

- [39] G. Onida, L. Reining, and A. Rubio, Electronic excitations: density-functional versus many-body Green's-function approaches, *Rev. Mod. Phys.* **74**, 601 (2002).
- [40] C. Hartwigsen, S. Goedecker, and J. Hutter, Relativistic separable dual-space Gaussian pseudopotentials from H to Rn, *Phys. Rev. B* **58**, 3641 (1998).
- [41] A. M. Koushki, R. Sadighi-Bonabi, M. Mohsen-Nia, and E. Irani, High-order harmonic generation of CO and N₂ molecules under linearly- and bi circularly-polarized laser pulses by TD-DFT, *Laser Phys.* **28**, 075404 (2018).
- [42] C. J. Joachain, N. J. Kylstra, and R. M. Potvliege, *Atoms in Intense Laser Fields* (Cambridge University Press, Cambridge, 2011).
- [43] F. Mauger, P. M. Abanador, T. D. Scarborough, T. T. Gorman, P. Agostini, L. F. DiMauro, K. Lopata, K. J. Schafer, and M. B. Gaarde, High-harmonic spectroscopy of transient two-center interference calculated with time-dependent density-functional theory, *Struct. Dyn.* **6**, 044101 (2019).
- [44] A. Fleischer, O. Kfir, T. Diskin, P. Sidorenko, and O. Cohen, Spin angular momentum and tunable polarization in high-harmonic generation, *Nat. Photon.* **8**, 543 (2014).
- [45] S.-M. F. Nee, C. Yoo, T. Cole, and D. Burge, Characterization for imperfect polarizers under imperfect conditions, *Appl. Opt.* **37**, 54 (1998).
- [46] O. Kfir, P. Grychtol, E. Turgut, R. Knut, D. Zusin, A. Fleischer, E. Bordo, T. Fan, D. Popmintchev, T. Popmintchev, H. Kapteyn, M. Murnane, and O. Cohen, Helicity-selective phase-matching and quasi-phase matching of circularly polarized high-order harmonics: Towards chiral attosecond pulses, *J. Phys. B* **49**, 123501 (2016).
- [47] E. D. Palik, Preface, in *Handbook of Optical Constants of Solids*, edited by E. D. Palik (Academic, Burlington, 1997), pp. xvii–xviii.
- [48] O. Kfir, S. Zayko, C. Nolte, M. Sivis, M. Möller, B. Hebler, S. S. P. K. Arekapudi, D. Steil, S. Schäfer, M. Albrecht, O. Cohen, S. Mathias, and C. Ropers, Nanoscale magnetic imaging using circularly polarized high-harmonic radiation, *Sci. Adv.* **3**, eaao4641 (2017).
- [49] J. Jilili, I. Tolbatov, F. Cossu, A. Rahaman, B. Fiser, and M. U. Kahaly, Atomic scale interfacial magnetism and origin of metal-insulator transition in (LaNiO₃)_n/(CaMnO₃)_m superlattices: A first principles study, *Sci. Rep.* **13**, 5056 (2023).
- [50] F. Siegrist, J. A. Gessner, M. Osslander, C. Denker, Y.-P. Chang, M. C. Schröder, A. Guggenmos, Y. Cui, J. Walowski, U. Martens, J. K. Dewhurst, U. Kleineberg, M. Münzenberg, S. Sharma, and M. Schultze, Light-wave dynamic control of magnetism, *Nature (London)* **571**, 240 (2019).
- [51] J. Hofbrucker, A. V. Volotka, and S. Fritzsche, Maximum elliptical dichroism in atomic two-photon ionization, *Phys. Rev. Lett.* **121**, 053401 (2018).
- [52] P. Lambropoulos, Multiphoton ionization of one-electron atoms with circularly polarized light, *Phys. Rev. Lett.* **29**, 453 (1972).
- [53] N. Mayer, S. Patchkovskii, F. Morales, M. Ivanov, and O. Smirnova, Imprinting chirality on atoms using synthetic chiral light fields, *Phys. Rev. Lett.* **129**, 243201 (2022).
- [54] G. Schönhense, Angular dependence of the polarization of photoelectrons ejected by plane-polarized radiation from argon and xenon atoms, *Phys. Rev. Lett.* **44**, 640 (1980).
- [55] J. E. Kruse, P. Tzallas, E. Skantzakis, C. Kalpouzos, G. D. Tsakiris, and D. Charalambidis, Inconsistencies between two attosecond pulse metrology methods: A comparative study, *Phys. Rev. A* **82**, 021402(R) (2010).
- [56] P. Balcou, P. Salières, A. L'Huillier, and M. Lewenstein, Generalized phase-matching conditions for high harmonics: The role of field-gradient forces, *Phys. Rev. A* **55**, 3204 (1997).
- [57] M. Bellini, C. Lyngå, A. Tozzi, M. B. Gaarde, T. W. Hänsch, A. L'Huillier, and C.-G. Wahlström, Temporal coherence of ultrashort high-order harmonic pulses, *Phys. Rev. Lett.* **81**, 297 (1998).
- [58] J. Peatross and D. D. Meyerhofer, Angular distribution of high-order harmonics emitted from rare gases at low density, *Phys. Rev. A* **51**, R906 (1995).
- [59] I. Orfanos, I. Makos, I. Lontos, E. Skantzakis, B. Förg, D. Charalambidis, and P. Tzallas, Attosecond pulse metrology, *APL Photonics* **4**, 080901 (2019).
- [60] I. Orfanos, I. Makos, I. Lontos, E. Skantzakis, B. Major, A. Nayak, M. Dumergue, S. Kühn, S. Kahaly, K. Varju, G. Sansone, B. Witzel, C. Kalpouzos, L. A. A. Nikolopoulos, P. Tzallas, and D. Charalambidis, Non-linear processes in the extreme ultraviolet, *J. Phys.: Photonics* **2**, 042003 (2020).
- [61] P. Tzallas, D. Charalambidis, N. A. Papadogiannis, K. Witte, and G. D. Tsakiris, Second-order autocorrelation measurements of attosecond XUV pulse trains, *J. Mod. Opt.* **52**, 321 (2005).
- [62] E. Hasović, W. Becker, and D. B. Milošević, Electron rescattering in a bicircular laser field, *Opt. Express* **24**, 6413 (2016).
- [63] G. Sansone, C. Vozzi, S. Stagira, and M. Nisoli, Nonadiabatic quantum path analysis of high-order harmonic generation: Role of the carrier-envelope phase on short and long paths, *Phys. Rev. A* **70**, 013411 (2004).
- [64] P. Salières, B. Carré, L. L. Déroff, F. Grasbon, G. G. Paulus, H. Walther, R. Kopold, W. Becker, D. B. Milošević, A. Sanpera, and M. Lewenstein, Feynman's path-integral approach for intense-laser-atom interactions, *Science* **292**, 902 (2001).
- [65] D. B. Milošević and W. Becker, Attosecond pulse trains with unusual nonlinear polarization, *Phys. Rev. A* **62**, 011403(R) (2000).
- [66] L. Barreau, K. Veyrinas, V. Gruson, S. J. Weber, T. Auguste, J.-F. Hergott, F. Lepetit, B. Carré, J.-C. Houver, D. Doweck, and P. Salières, Evidence of depolarization and ellipticity of high harmonics driven by ultrashort bichromatic circularly polarized fields, *Nat. Commun.* **9**, 4727 (2018).
- [67] P. Antoine, A. L'Huillier, M. Lewenstein, P. Salières, and B. Carré, Theory of high-order harmonic generation by an elliptically polarized laser field, *Phys. Rev. A* **53**, 1725 (1996).
- [68] S. Chatziathanasiou, I. Lontos, E. Skantzakis, S. Kahaly, M. U. Kahaly, N. Tsatrafyllis, O. Faucher, B. Witzel, N. Papadakis, D. Charalambidis, and P. Tzallas, Quantum path interferences in high-order harmonic generation from aligned diatomic molecules, *Phys. Rev. A* **100**, 061404(R) (2019).
- [69] M. U. Kahaly and U. V. Waghmare, Contrast in the electronic and magnetic properties of doped carbon and boron nitride nanotubes: A first-principles study, *J. Phys. Chem. C* **112**, 3464 (2008).

Correction: The name of the sixth author was misspelled and has been fixed.